IEEE Robotics and Automation Letters (RA-L) paper, presented at ICRA 2024, Yokohama, Japan. Cite as RA-L paper.

Development of an easy-to-cut six-axis force sensor

Takamasa Kawahara[1] *Student Member, IEEE,*, Toshiaki Tsuji[2] *Senior Member, IEEE,*

***Abstract*—Although the potential demand for force sensors in both robotics and automation is high, the complexity of their structure increases the number of manufacturing processes. As a result, the rising cost of sensors has hindered the practical application of force measurement and force control. In this study, a flexure element is proposed, consisting of a structure that is easier to cut and process than conventional ones. Additionally, holes through the side of a cuboid are incorporated to simplify the manufacturing of force sensors. To ensure the safety of the proposed sensor design, an approximate equation is derived to predict the maximum von Mises stress on the flexure element using design parameters. Subsequently, we clarified a way to attach the strain gauge in a position that improves sensitivity. The results of the actual prototype sensor based on the proposed method show that the maximum nonlinearity error and decoupling error in the other axes are 0.442 %R.O. and 0.660 %R.O., respectively, and the performance is comparable to that of conventional force sensors. Because the prototype has a difference in resolution between the axes, a method for improving the resolution isotropy without changing the difficulty of machining is also proposed. In addition, the validity of the proposed method is demonstrated using experiments. Consequently, a force sensor with the same level of performance was developed using the proposed method, and the cutting process was made easier compared to that of conventional methods. This research is expected to lead to lower cost force sensors in the future.**

***Index Terms*—Force and Tactile Sensing, Force Control.**

I. Introduction

SIX-AXIS force sensors are used to detect forces and moments in all three axes in a three-dimensional space, and are typically attached to a robot that interacts with the environment and humans [1]–[3]. Force control using force sensors dramatically improves the performance of robots, and the demand for force sensors is increasing in a wide range of fields such as aerospace, medical, and civil engineering. There are various types of force detection methods for force sensors, such as the strain gauge-type [4]–[6] and capacitance-type [7]–[9]. Capacitance-type sensors are relatively easy to manufacture, and much of the literature focuses on simplifying the manufacturing process [7]. However, capacitance-type sensors are affected by hysteresis [10]. Thus, strain gauge force sensors are the most common type of accurate sensors. Strain gauge-type six-axis force sensors contain a flexure element, and it is possible to estimate the external force based on the amount of detected strain by attaching strain gauges to the flexure element.

Although the potential demand for six-axis force sensors is significant, their usage is currently limited to applications such as grinding, deburring in industrial automation, and piece-picking due to the high cost of the sensor units. The main reason for this is the manufacturing cost, wherein a lot of the costs are spent on cutting the complex structure of the flexure element. Fig. 1 shows an example of a typical strain gauge-type six-axis force sensor structure, based on a study by Jack *et al.* [11]. There are three typical types of strain gauge-type six-axis force sensors, cross beam-type (Fig. 1a), parallel structure-type (Fig. 1b), and column-type (Fig. 1c). The cross beam-type has a flexible support beam between the inner and outer structures, and has been employed in several studies [12], [13]. When an external force is applied to the inner structure, strain gauges attached to the beam react, allowing the estimation of the external force. The cross beam-type has a monolithic structure, which provides high stiffness and reliability. The parallel structure-type has a structure in which six or more limbs with spherical joints are fixed to the top plate and base. When an external force is applied from the top plate, axial strain is generated in the limbs, and the amount of strain can be measured to estimate the external force. Its has a high load resistance owing to load distribution to the limbs. Various studies have been conducted on the optimization of the sensitivity isotropy in the strain gauge-type recently, mainly using the parallel structure-type [14], [15]. However, all the different types are complex, and they require very difficult machining. The column-type has a simpler structure than the cross beam and parallel structure-types. Thus, it is easier to manufacture, which has been argued in some studies [16], [17]. However, the stiffness of the column-type is much higher in the vertical direction than in the other directions owing to its structure, and it is difficult to uniformly adjust the sensitivity between the axes. Thus, there is still no force sensor type that has good resolution isotropy in each axis and is easy to manufacture.

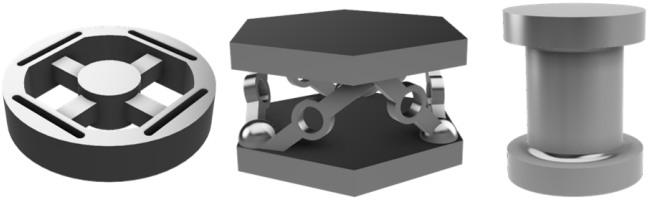

(a)Cross beam-type (b)Parallel structure-type (c)Column-type

Fig. 1. An example of a typical of six-axis force semsor structure with strain gauge-type

Manuscript received: July 27, 2023, Year; Revised: September 12, 2023; Accepted: November 5, 2023

This paper was recommended for publication by Editor Clement Gosselin upon evaluation of the Associate Editor and Reviewers' comments. *This work was supported in part by JSPS KAKENHI, Japan Grant Number 21H01280.

[1,2]T. Kawahara and T. Tsuji are with the Dept. Electrical Engineering, Electronics and Applied Physics, Saitama University, 255 Shimo-okubo, Sakura, Saitama, 338-8570, Japan (email:t.kawahara.376@ms.saitama-u.ac.jp, tsuji@ees.saitama-u.ac.jp)

Digital Object Identifier (DOI): see top of this page.

IEEE Robotics and Automation Letters (RA-L) paper, presented at ICRA 2024, Yokohama, Japan. Cite as RA-L paper.

IEEE Robotics and Automation Letters (RA-L) paper, presented at ICRA 2024, Yokohama, Japan. Cite as RA-L paper.

Thus far, the general properties of each type of strain gauge-type six-axis force sensor have been described. Subsequently, the previous studies on strain gauge-type force sensors that consider the manufacturing cost of force sensors are introduced. Ubeda *et al.* proposed a one-axis torque sensor that does not require complicated cutting work or special tools, and can be manufactured only by a one-axis cutting feed motion [18]. Yao *et al.* fabricated a six-axis force sensor with a parallel structure comprising eight limbs arranged in parallel using metal 3D printing [19]. Complex structures can be easily manufactured using metal 3D printing and the cost can be reduced by automating the manufacturing process. However, the machining accuracy and forming speed of metal 3D printers are inferior to those of cutting technology. Moreover, there is no research on six-axis force sensors that can be manufactured only by a one-axis cutting feed motion.

In this study, a new type of force sensor is proposed by drastically changing the structure of the flexure element to simplify the cutting process. The structure of the flexure element is very simple, and comprises holes through the side of a cuboid. Cutting can only be done by drilling and tapping using a one-axis motion, which means that expensive tools are not required and machining is easy. Moreover, it is possible to measure the forces and moments in the six-axis with high accuracy, by attaching strain gauges to the proposed flexure element, at appropriate positions.

The remainder of this paper is organized as follows. First, the structure of the flexure element, its design method, and a method for improving the sensitivity isotropy are described in Section Ⅱ. Subsequently, the performance evaluation of the force sensor manufactured based on the proposed method is described in Section Ⅲ. Finally, Section Ⅳ concludes the paper.

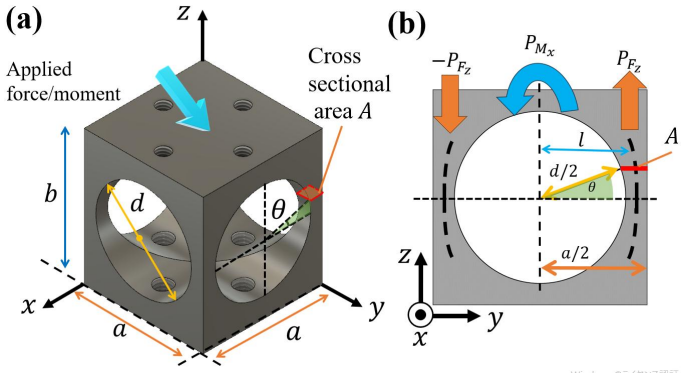

Fig. 2. Proposed flexure element structure

II. Design Methods for the Proposed Sensor

This section describes the structure and design method of the proposed sensor, and the method for attaching the strain gauges for force sensing. In addition, the sensitivity of the proposed flexure element varies between axes owing to its structure. The improvement method is also presented.

A. Structure of the flexure element

Fig. 2 shows an overview of the proposed flexure element. It has a simple structure, consisting of a cuboid with a width and length a, height b, and holes of diameter d drilled through the centers of the front, back, left, and right sides. The proposed flexure element can be cut using only the linear motion of the principal spindle of the machine. It can be manufactured by first tapping in the XY plane, then rotating the plane and drilling in the ZY and ZX planes. It can be manufactured using only one-axis motion of drilling and tapping, and does not require complex numerically-controlled machining without employing the synchronous motion of two or more axes. In other words, manufacturing is easier than conventional methods because only drilling is required for cuboid, and the introduction of a large complex machine such as a CNC(Computerised Numerical Control) machine is not necessary. Hereafter, the proposed flexure element will be referred to as multi-hole cuboid.

B. Design method for the multi-hole cuboid

It is important to understand the stress in the flexure element when a load is applied to prevent rupture and permanent deformation. Therefore, the design in this study is based on the von Mises yield condition to ensure the safety of the sensor. The maximum von Mises stress that occurs when a force or moment is applied to a flexure element was assumed to be σ_e MPa, and the yield stress of a material used for a flexure element was assumed to be σ_y MPa. Based on the von Mises yield condition, permanent deformation occurs in a flexure element when $\sigma_e = \sigma_y$. Therefore, a sensor must be designed to satisfy $\sigma_e < \sigma_y$, when the rated load is applied.

Therefore, an approximate equation is derived to estimate the maximum von Mises stress σ_e that occurs when a given load is applied to a multi-hole cuboid of arbitrary shape. We now determine the stress applied to the cross sectional area A in Fig. 2. If a force P_{F_z} is applied in the Z-axis to the flexure element, the length of one side of the cross sectional area A is $\frac{a}{2} - \frac{d}{2}cos\theta$, so the vertical stress σ_{zz} acting on the Z-axis is given by the following equation.

$$\sigma_{zz} = \frac{|P_{F_z}|}{\left(\frac{a}{2} - \frac{d}{2}cos\theta\right)^2} \tag{1}$$

If vertical stresses and shear forces other than σ_{zz} are negligibly small in the microelements near the hole, the von Mises stress can be regarded as equivalent to σ_{zz}. On the other hand, stress is concentrated in near the hole and vertical stresses are stronger than σ_{zz}. Then the maximum von Mises stress σ_{eF_z} can be expressed in a simplified eqation as follows:

$$\sigma_{eF_z} = \alpha|\sigma_{zz}| = \frac{|P_{F_z}|}{\frac{1}{\alpha}\left(\frac{a}{2} - \frac{d}{2}cos\theta\right)^2} = \frac{|P_{F_z}|}{w_{0_{F_z}}ad + w_{1_{F_z}}a^2 + w_{2_{F_z}}d^2} \tag{2}$$

α is the stress concentration factor. w is a coefficient that contains information on the position θ in the flexure element and the stress concentration α. Therefore, the value of the coefficient w changes if the load-application axis differs. In

IEEE Robotics and Automation Letters (RA-L) paper, presented at ICRA 2024, Yokohama, Japan. Cite as RA-L paper.

this study, the coefficient w_{F_z} is expressed for the case when P_{F_z} is applied. Next, the stress when the moment P_{M_x} is applied to the cross sectional area A is determined. As shown in Fig. 2(b), the distance l from the center of the sensor to the center of the column can be expressed by the following equation in the ZY plane.

$$l = \frac{d}{2}cos\theta + \frac{\frac{a}{2} - \frac{d}{2}cos\theta}{2} = \frac{a}{4} + \frac{d}{4}cos\theta \tag{3}$$

When the moment P_{M_x} is applied, it is considered that only the force P_{F_z} is acting on the column. Since $P_{F_z} = P_{M_x}/l$, and assuming the same conditions as in the case of P_{F_z}, the maximum von Mises stress σ_{eM_x} is determined by Eq. (2).

$$\begin{aligned}\sigma_{eM_x} &= \frac{|P_{F_z}|}{\frac{1}{\alpha}(\frac{a}{2} - \frac{d}{2}cos\theta)^2} = \frac{|P_{M_x}|}{\frac{1}{\alpha}(\frac{a}{4} + \frac{d}{4}cos\theta)(\frac{a}{2} - \frac{d}{2}cos\theta)^2} \\ &= \frac{|P_{M_x}|}{w_{0_{M_x}}da^2 + w_{1_{M_x}}ad^2 + w_{2_{M_x}}a^3 + w_{3_{M_x}}d^3}\end{aligned} \tag{4}$$

By the concise modeling described above, the approximate eqation for the maximum von Mises stress can be expressed in a simple eqation with equal dimensions on both sides, as in Eq. (2) and (4). When $P_{F_x}, P_{F_y}, P_{M_y}, P_{M_z}$ are applied, the approximate eqation for the maximum von Mises stress can also be expressed with equal dimensions on both sides, as defined by the following eqation.

$$\sigma_{eF_x} = \frac{|P_{F_x}|}{w_{0_{F_x}}ad + w_{1_{F_x}}a^2 + w_{2_{F_x}}d^2} \tag{5}$$

$$\sigma_{eM_z} = \frac{|P_{M_z}|}{w_{0M_z}da^2 + w_{1M_z}ad^2 + w_{2M_z}a^3 + w_{3M_z}d^3} \tag{6}$$

The design in the F_y and M_y directions can be conducted in the same way as that for F_x and M_x since the multi-hole cuboid is a point-symmetric structure. By obtaining the coefficient w, it is possible to estimate the maximum von Mises stress in each axis when a load is applied.

The procedure for obtaining the coefficient w is as follows:

1. Create several models for multi-hole cuboids with different sizes (sides and holes) in simulation, and calculate the maximum von Mises stress when a constant load is applied to the models.
2. Create 3D scatter diagrams of the calculated maximum von Mises stresses, sides, and holes.
3. Perform multiple regression analysis based on the 3D scatter diagram, and obtain the coefficient w by approximating Eq. (2),(4)-(6).

For simplicity, the case of a cube with equal side widths, lengths and heights a and a hole of diameter d was considered and models were created to determine the coefficient w. Explanations are given in the following order.

1) Calculation of maximum von Mises stress: The model was created and simulated using Fusion360 (Autodeck, Inc.). The model comprised tetrahedral elements having ten nodes. The procedure for simulation and acquisition of calculated values is described below.

(i) 40 models are created for cubes with sides a of 30, 40, 50 and 60 mm; and different sizes with side hole diameter d ratios of 0.1, 0.2, $\cdots$, 0.8, 0.9 and 0.95. The ratio represents the diameter of the hole d in relation to the size of one side a.

(ii) The maximum von Mises stresses are calculated by entering the model material, boundary conditions and applied loads. In this case, the applied loads are as follows: $F_x = 500$ N, $F_z = 1000$ N, $M_x = 100$ Nm, and $M_z = 100$ Nm, the material used is aluminum 7075.

(iii) Procedure (ii) on each model, and four axes are applied per model, for a total of 160 calculated values.

The stress distribution in the multi-hole cuboid under applied load is shown in Fig. 3, using F_x as an example. It can be seen that the maximum von Mises stress appears at different points for different ratios. Specifically, between the ratios of 0.1 and 0.3, the maximum von Mises stress appears near the bottom, whereas for ratios of 0.4 and above, the maximum von Mises stress appears near the hole. This is because the maximum stress appearing in the entire cube is larger than the stress concentration appearing locally near the hole when the diameter of the hole is small.

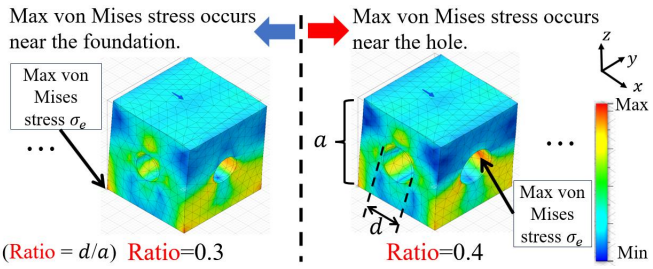

Fig. 3. Stress distribution of the flexure elements under load application in the F_x direction.

2) Creation of 3D scatter diagrams: The relationship between the calculated maximum von Mises stress, side, and hole size is represented in the 3D scatter diagram, as shown in Fig. 4. In Fig. 4, the calculation points are plotted in red when the maximum von Mises stress appears near the hole and in blue when it appears near the bottom. Here, Eq. (2) is transformed into Eq. (7) to conduct multiple regression analysis based on the 3D scatter diagrams

$$w_{0_{F_z}}ad + w_{1_{F_z}}a^2 + w_{2_{F_z}}d^2 = \frac{|P_{F_z}|}{\sigma_{eF_z}} \tag{7}$$

A similar transformation is made in the Eq. (4)-(6). In (7), a and d are explanatory variables and $|P|/\sigma_e$ is the objective variable. The coefficient w is obtained through multiple regression analysis using these variables. The red and blue calculation points show different trends in the appearance of the maximum von Mises stress. It can be seen that the maximum von Mises stress appears in the near of the hole when the ratio is greater than 0.4 for F_x, greater than 0.5 for M_z, and greater than 0.6 for M_x. Therefore, an approximate equation is obtained in the range with a ratio of 0.6 or more, and the coefficient w is determined.

IEEE Robotics and Automation Letters (RA-L) paper, presented at ICRA 2024, Yokohama, Japan. Cite as RA-L paper.

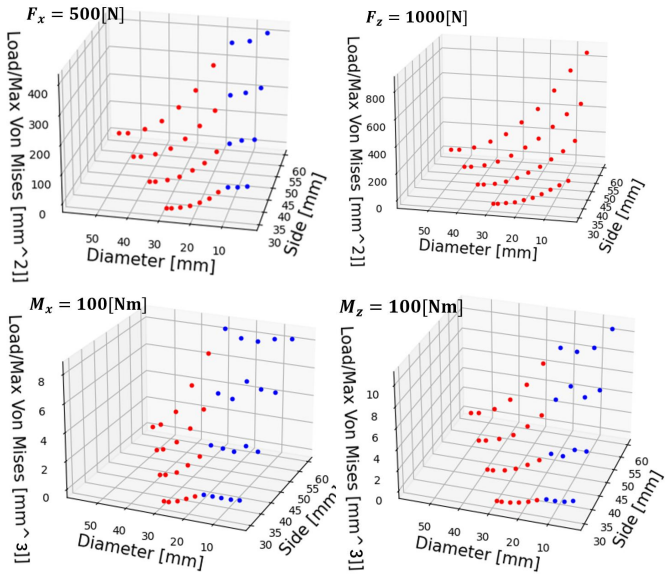

Fig. 4. 3D scatter diagram of the $|P|/\sigma_e$

3) Determination of the coefficient w: Multiple regression analysis is performed based on the 3D scatter diagram. The values of w and RMSE are shown in Table I, and the approximate surfaces are shown in Fig. 5. The fact that the RMSE is sufficiently small, indicates that the approximate equations (2),(4)-(6), can be used to estimate the maximum von Mises stress value with a high degree of accuracy and are reliable enough for use in design.

TABLE I
VALUES OF THE COEFFICIENT w AND RMSE

	F_x	F_z	M_x	M_z
w_0	-0.483	-0.606	-2.29 E-5	-22.5 E-5
w_1	0.230	0.298	-25.7 E-5	9.93 E-5
w_2	0.254	0.308	9.54 E-5	11.4 E-5
w_3			18.6 E-5	1.19 E-5
RMSE	0.559	0.773	0.223 E-1	0.806 E-2

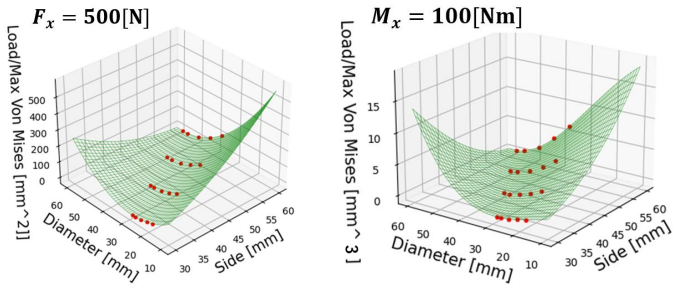

Fig. 5. Approximate surfaces of the 3D scatter plots (examples for F_x and M_x)

The maximum von Mises stress σ_e can be estimated for any shape and external force by substituting the values of w into Eq. (2),(4)-(6). However, the applicable range is $30 \leq a \leq 60, 0.6a \leq d < a$. Finally, the safety of the sensor under load application can be determined by comparing σ_e with the yield stress σ_y of the material.

C. Strain gauge attachment position

All strain gauges perpendicular to the bottom were uniformly attached and the strain distribution in the perpendicular direction was examined. Fig. 6 shows the amount of strain in the perpendicular direction, with red representing the tension and blue the compression. Thus, the strain distribution in the multi-hole cuboid is non-uniform across its surface. However, the relationship between the applied load and the strain remains highly linear at any location on the flexure element surface. Therefore, by placing the strain gauges at points of high strain, it is possible to measure with high sensitivity while maintaining linearity. The amount of strain can be estimated using Finite Element Analysis(FEA), and the optimal attachment positions can be determined based on values derived from simulations. As shown in Fig. 6, different axes are prone to localized distortion in different areas, and the strain tends to appear in the thinnest areas of the column for F_z, M_x and M_y, and at slight offsets from the thinnest areas of the column for F_x, F_y, and M_z. This is because normal forces (F_z, M_x, M_y) and shear forces (F_x, F_y, M_z) have different stress concentration areas. To attach the strain gauges to the areas where a large amount of strain is shown, the characteristic that the maximum amount of strain changes for each axis is utilized. As shown in Fig. 7, the inner strain gauges are attached at half the height from the bottom (the thinnest areas of the column) to improve the sensitivity of the F_z, M_x and M_y axes. The outer strain gauges are attached a little lower than the inner strain gauges (at slight offsets from the thinnest areas of the column) for the F_x, F_y and M_z axes. The measurement circuit is shown in Fig. 8. A quarter-bridge system was used for the measurement circuit to detect 16 output voltages using 16 strain gauges, from $r1$ to $r16$. The 16 outputs were passed through a calibration matrix to measure the forces and moments in six-axis.

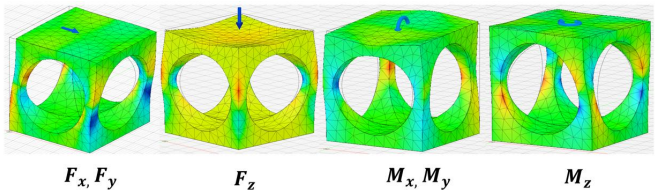

Fig. 6. Deformation and strain distribution in the flexure element

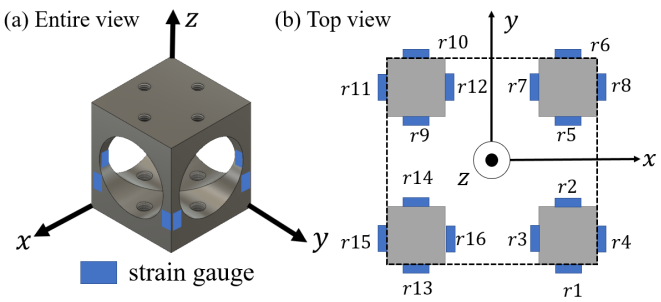

Fig. 7. Strain gauge arrangement diagram

Subsequently, the position of the outer strain gauges are

IEEE Robotics and Automation Letters (RA-L) paper, presented at ICRA 2024, Yokohama, Japan. Cite as RA-L paper.

explained in detail. The variables shown in Eq. (8) were defined to identify the position of the outer strain gauges $(i = 1, 4, 6, 8, 10, 11, 13, 15)$.

$$\alpha_i = \left|\frac{e_{pi}}{e_{oi}}\right| = \left|\frac{E \cdot K \cdot \varepsilon_{pi}/4}{E \cdot K \cdot \varepsilon_{oi}/4}\right| = \left|\frac{\varepsilon_{pi}}{\varepsilon_{oi}}\right| \tag{8}$$

Where E is bridge voltage, K is the gauge factor, and $\varepsilon_{pi}, \varepsilon_{oi}$ is the amount of strain detected by the strain gauge r_i. Where e_{pi} is the value of the output voltage e_i for the case where the strain gauges facing each other are different in terms of the height from the bottom, as shown in Fig. 9. e_{oi} is, as a comparison, the value of output voltage e_i when the strain gauges are placed facing each other at the thinnest areas of the column, and the height from the bottom is the same. In other words, α_i is the ratio of the output voltage e_i for different strain gauge attachment heights. A higher output voltage can also be obtained by attaching the strain gauge at a position where α_i is large. α_i can be obtained by measuring the amount of strain in the perpendicular direction when the load is applied via FEA. Through these processes, it is possible to identify the attachment position with good sensitivity.

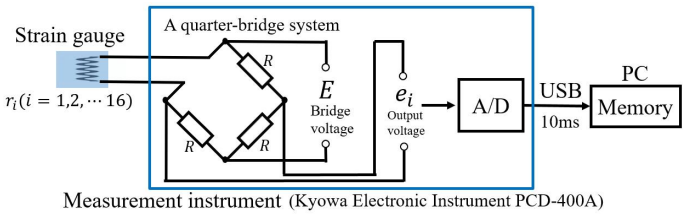

Fig. 8. Connection diagram for the strain gauges and measurement instrument

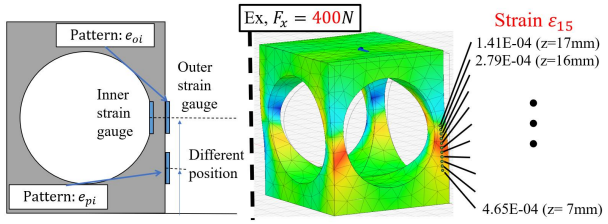

Fig. 9. Position of the strain gauges viewed from the side and the amount of strain ε_{15} was calculated (example for F_{x})

D. Methods for improving the sensitivity isotropy

Multi-hole cuboids are structurally stiffer in the Z-axis compared to the other axes. This causes a difference in sensitivity between the axes. To make the sensor suitable for a wide range of applications, it is better to achieve a uniform sensitivity in each axis. Some research exists that focuses on optimizing the isotropy of sensitivity [9]. Herein, methods for improving the sensitivity isotropy and their design methods are described. To improve the sensitivity isotropy, the width and length can be increased and the stiffness in the Z-axis can be reduced without changing the height of the multi-hole cuboid, as shown in Fig. 10. This is because the distance between the center of gravity of the load applied to the top plate and the column varies with the width, and the moment load applied to the column increases when the F_{z} load is applied with the same amount. In addition, although the machining procedure for the width-long type (Fig. 10 right) increases compared to that of the original type (Fig. 10 left), the difficulty in cutting is not significantly affected because it does not require the synchronized motion of the tool in more than two axes. Subsequently, a method for determining the width of the sensor (width-long type) such that the sensitivies of both axes are equal when the same amount of load is applied to F_{z}, F_{x}, and F_{y}, respectively, is described. The value expressed in Eq. (9) is introduced during the design stage as an indicator for evaluating the sensitivity between axes using FEA.

$$\|\varepsilon\| = \sqrt{\sum_{i=1}^{n} \varepsilon_i^2}, \tag{9}$$

where $\|\varepsilon\|$ is the Euclidean norm of the amount of strain ε_i measured by the strain gauge r_i when a load is applied to the sensor. Additionally, $\|\varepsilon\|$ is a scalar quantity that represents the projection of the strain matrix $\boldsymbol{\varepsilon} = \begin{bmatrix} \varepsilon_1 & \varepsilon_2 & \varepsilon_3 & \dots & \varepsilon_n \end{bmatrix}^{\mathrm{T}}$ onto a single dimension. It shows how much the sensor is susceptible to distortion under load. Moreover, it is useful for designing because it is not necessary to compare the responses of multiple strains, and only one value can be used. Because the proposed sensor uses 16 strain gauges, $i = 16$. It is necessary to determine the flexure element width at which the $\|\varepsilon_{F_{\mathrm{y(x)}}}\|$ and $\|\varepsilon_{F_{\mathrm{z}}}\|$ measured when the same amount of load is applied in the $F_{\mathrm{y(x)}}$ and F_{z} directions. Herein, FEA was used to calculate the ε_i.

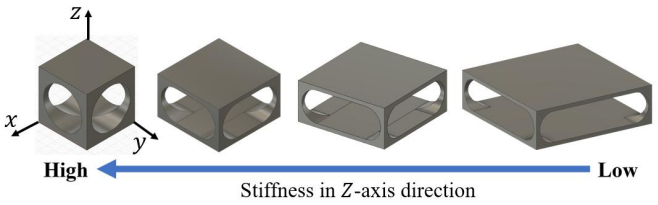

Fig. 10. Stiffness along the Z-axis under varying widths

III. Manufacturing the Prototype Sensor and the Experimental Results

In this section, the manufacturing of two prototype sensors, one similar to the one shown in Fig. 2 and the other similar to the one shown in Fig. 10, are presented along with their performance evaluation results. Hereafter, the prototype sensor of the original type (Fig. 2) is refferred to as "A" and the prototype sensor of the width-long type (Fig. 10 right) is denoted as "B".

A. Design of prototype sensor-A and B

Based on the method described in Section II-B, the size of the flexure element for sensor-A was determined. Aluminum alloy 7075, a material that is easy to cut and has high strength, was used as the material for sensor-A. As an index for determining the size, the design should be as small as possible but with a large rated load and high load resistance. When

IEEE Robotics and Automation Letters (RA-L) paper, presented at ICRA 2024, Yokohama, Japan. Cite as RA-L paper.

evaluating the static performance, it is generally considered desirable for light metal materials to have a safety factor of 5.00 or more with respect to the static load. Therefore, sensor-A was designed to have a safety factor of 7.00 or more for the rated load, with $a = 30$ mm, and the rated load as $F_{\mathrm{x}} = F_{\mathrm{z}} = 400$ N and $M_{\mathrm{x}} = M_{\mathrm{z}} = 7$ Nm. Under these conditions, the range of hole diameter d was determined using the F_{x} axis as an example.

Substituting the values of $w_{F_{\mathrm{x}}}$ in Table I into Eq. (5), $a = 30$ and $P_{F_{\mathrm{x}}} = 400$, Eq. (10) is obtained as:

$$\sigma_{eF_{\mathrm{x}}} = \frac{|400|}{0.254 d_{F_{\mathrm{x}}}^2 + (-0.483 \times 30 d_{F_{\mathrm{x}}}) + 0.230 \times 30^2}, \quad (10)$$

where $d_{F_{\mathrm{x}}}$ is the design parameter of the hole in the F_{x} axis. From the scope of application of (2), $18 \leq d < 30$. Because the yield stress of aluminum alloy 7075 is 505 MPa, the following condition must be satisfied to obtain a safety factor of 7.00 or more.

$$\sigma_{eF_{\mathrm{x}}} < 505/7.00 \quad (11)$$

The range of $d_{F_{\mathrm{x}}}$ can be determined by solving the inequalities of $d_{F_{\mathrm{x}}}$, which are obtained from Eq. (10) and (11), resulting in $18 \leq d_{F_{\mathrm{x}}} \leq 24.0$. Similarly, the ranges of $d_{F_{\mathrm{z}}}, d_{M_{\mathrm{x}}}$, and $d_{M_{\mathrm{z}}}$ were determined for the other axes as $18 \leq d_{F_{\mathrm{z}}} \leq 25.2, 18 \leq d_{M_{\mathrm{x}}} \leq 25.7$, and $18 \leq d_{M_{\mathrm{z}}} \leq 24.1$, respectively. Based on the conditions for $d_{F_{\mathrm{x}}}, d_{F_{\mathrm{z}}}, d_{M_{\mathrm{x}}}$ and $d_{M_{\mathrm{z}}}$, d is greater than 18.0 mm and less than or equal to 24.0 mm; thus, a strength with a safety factor of 7.00 or greater can be guaranteed when the rated load is $F_{\mathrm{x}} = F_{\mathrm{z}} = 400$ N, and $M_{\mathrm{x}} = M_{\mathrm{z}} = 7$ Nm.

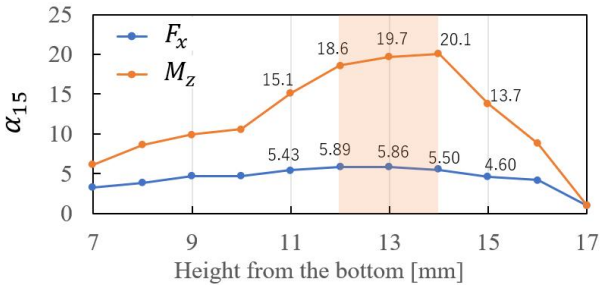

Fig. 11. Changes in α_{15} owing to changes in the position of the attachment.

The final size of sensor-A was a width and length of 30 mm, a height of 34 mm, and a hole diameter of 24 mm. The rated load and safety factor calculated during simulation are shown in Table II. Despite its small size, the design has a wide measuring range and is sufficiently robust, with a safety factor of more than 7.0. The height is 4 mm higher than the width and length because the design accounts for the depth of the screws used to fix the top board to the base.

Subsequently, the attachment positions of the outer strain gauges on sensor-A are explained. As described in Section II-C, the outer strain gauges were attached at slight offsets from the thinnest areas of the column. The amount of strain that appeared when $F_{\mathrm{x}} = 400$ N, and $M_{\mathrm{z}} = 7$ Nm were applied to a model of the same size and material as sensor-A was measured, as shown in Fig. 9. By obtaining α_i using the calculated values and Eq. (8), the position where the output voltage strongly appears can be identified. When F_{x} is applied, the output voltages e_4, e_8, e_{11}, and e_{15} increase; and when F_{y} is applied, the output voltages e_1, e_6, e_{10}, and e_{13} increase. For M_{z}, all output voltages of the outer strain gauges increase. Because the multi-hole cuboid is a point-symmetrical structure, it was assumed that the same results are obtained for other α when one model is used; thus, the position of the strain gauge r_{15} was investigated using α_{15} as a model. The amount of strain was calculated at heights of $7, 8, \ldots 17$ mm from the bottom. The relationship between the mesurmed position and α_{15} is shown in Fig. 11. As shown in Fig. 11, the value of α remains almost the same in the 12-14 mm range. On the other hand, the value of α decreases significantly below 12 mm and above 14 mm. Assuming that the manual attachment of the gauges is subject to misalignment within ± 1 mm, the strain gauges were attached at the median position of 13 mm in this experiment. For these reasons, the position of the strain gauges was determined by taking into account simulation-based values and manufacturing reasons.

Based on the above, the actual flexure element and sensor-A are shown in Fig. 12. The strain gauges (Kyowa Electronic Instruments KFGS-03-120-C1-23) that had a width of 2.4 mm and height of 3.4 mm were used. The weight of the flexure element was as light as 34 g because, structurally, it loses most of its mass in the cutting process.

Subsequently, Fig. 12 shows the actual width-long type sensor (sensor-B), whose width was determined based on the method described in Section II-D. The material, height, diameter of the hole, and thickness of the thinnest part of the column are the same as those of sensor-A. The rated load and safety factor are given in Table II. To ensure a fair evaluation of the performance of sensor-A and B, the rated load was purposely set to the same value as that of sensor-A. The strain gauges were also attached at the same position as in the case of the sensor-A.

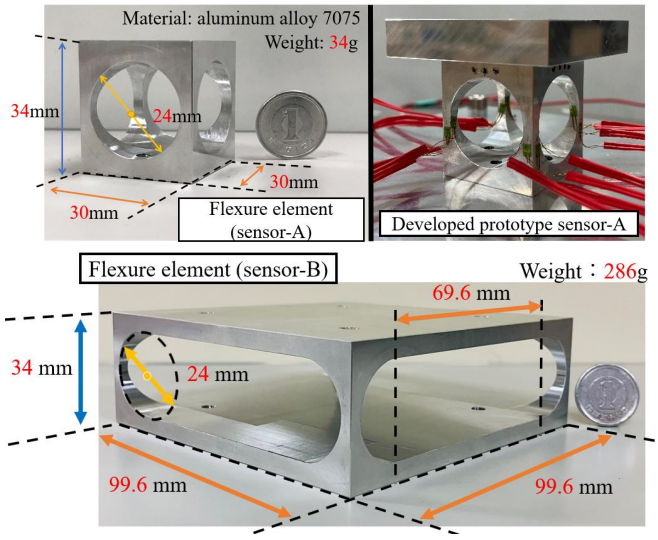

Fig. 12. Flexure element and developed prototype sensor-A and B

IEEE Robotics and Automation Letters (RA-L) paper, presented at ICRA 2024, Yokohama, Japan. Cite as RA-L paper.

B. Performance evaluation results

The performance evaluation results of sensor-A and B are presented in this section. In this experiment, the performance was evaluated in terms of nonlinearity error (NE), decoupling error (DE), repeatability error (RE) and hysteresis error (HE). The four performance were obtained by applying a load to the sensors under the conditions described as follows.

In X,Y-axes:

F1 $0.00, \pm12.5, \pm25.0, \pm50.0, \pm100, \pm200, \pm300$ N

M1 $0.00, \pm0.50, \pm1.25, \pm2.5, \pm3.75, \pm6.25, \pm11.25$ Nm

In Z-axis:

F2 $0.00, \pm12.5, \pm25.0, \pm50.0, \pm100, \pm200, \pm400$ N

M2 $0.00, \pm0.24, \pm0.60, \pm0.96, \pm2.16, \pm5.16$ Nm

NE is the maximum deviation from the straight line connecting the base point of the calibration curve and the rated load point when a load is applied, and it is expressed as a percentage of the rated load. Meanwhile, DE is an index representing the response of the output of a component other than the applied load. RE is an index of the deviation between successive measurements under the same load and conditions, while HE is an index of the deviation when unloading after the load has been applied. The results for NE, DE and HE were calculated as the average of five loadings, while RE was calculated as the maximum deviation when five loadings. Additionally, NE, DE, and RE were evaluated by incrementally applying loads in ascending order of magnitude for conditions F1, F2, M1, and M2. For HE, the evaluation was conducted by unloading sequentially after applying the maximum load for each condition. PCD-400A(Kyowa Electronic Instrument) was used for data collection. As shown in Fig. 8, PCD-400A converts the signals output from the strain gauges into A/D signals and transmits them continuously to the PC.

Table II shows the respective largest values of NE, DE, RE, and HE. Fig. 13 shows the F_{x} with the largest DE and the M_{z} with the largest RE for sensor-A. For sensor-B, the F_{z} with the largest RE is also shown. An enlarged section of the area with significant errors is also displayed in Fig. 13. The performance of NE, DE and HE was less than 2.00 %R.O. for both sensor-A and B. Considering that the performance required for commercial force sensors is 1.75 to 1.00 %R.O., the performance of the prototype sensors was comparable to that of commercial force sensors [10]. On the other hand, the RE was a maximum of 4.00 %R.O. or higher for both sensor-A and B.

C. Resolution

There are various methods to determine resolution, which can be chosen arbitrarily. However, it is not possible to measure signals smaller than the stationary noise. Since the actual measurement performance varies even if the resolution is set to a finer level than the noise. In this study, following the approach of previous studies for force sensors, we defined the resolution to be of the same value as the stationary noise [20]. Fig. 14 shows the change in the S/N ratio for $F_{\mathrm{x}}, F_{\mathrm{y}}$, F_{z}, which was calculated using Eq. (12).

$$SNR = 20\log_{10}\frac{L_{\mathrm{true}}}{\sqrt{HN^2 + NE^2 + DE^2}} \qquad (12)$$

L_{true} is the actual true value of the applied load, HN is the high-frequency noise (0.03 % R.O.), NE is the nonlinearity error; and DE is the decoupling error, which provides results on all noises. The resolution were obtained by applying a load to the sensors under the conditions described as follows.

In X,Y,Z-axes:

$0.00, 0.100, 0.200, \cdots 0.900, 1.00, 1.50, \cdots 6.50, 7.00$ N

When it exceeds 0 dB, the measurement value exceeds the noise; therefore, the measurement value at this point was set as the resolution. For sensor-A, there is a difference between the resolution in the X,Y-axes and Z-axis. Specifically, the X,Y-axes and Z-axis resolutions of sensor-A were 0.800, 0.600, and 2.00 N, respectively, while those of sensor-B were 0.900, 1.50, and 2.00 N, respectively. These results indicate that sensor-B has better balance of the resolutions. In addition, the SNR of the Z-axis in the sensor-B at 5.00 N is more than twice better than that in sensor-A. From the above, it is clear that the resolution isotropy can be improved without changing the measurement accuracy, by adjusting the width of the flexure element.

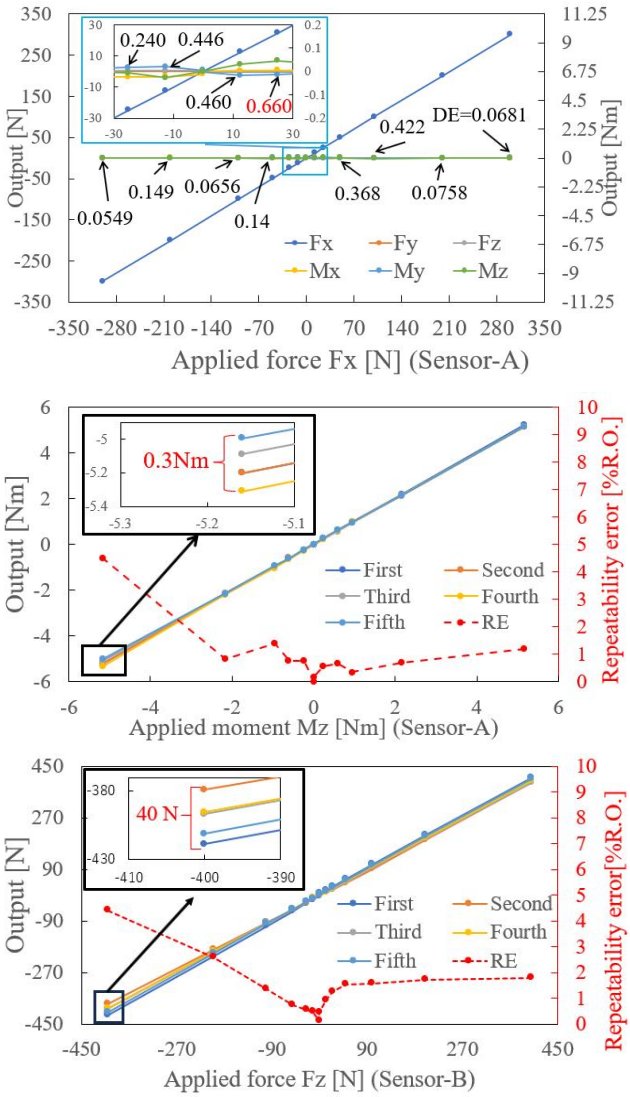

Fig. 13. Static responses of prototype sensor with respect to a single directional force or moment

IEEE Robotics and Automation Letters (RA-L) paper, presented at ICRA 2024, Yokohama, Japan. Cite as RA-L paper.

IEEE Robotics and Automation Letters (RA-L) paper, presented at ICRA 2024, Yokohama, Japan. Cite as RA-L paper.

TABLE II
PERFORMANCE OF PROTOTYPE SENSOR-A AND B

Sensor	A						B					
Axis	F_x	F_y	F_z	M_x	M_y	M_z	F_x	F_y	F_z	M_x	M_y	M_z
Rated load	400 N		900 N	15 Nm		7 Nm	400 N		900 N	15 Nm		7 Nm
Safety factor	7.35		7.14	7.59		7.79	9.13		3.48	15.0		15.0
NE [%R.O.]	0.442	0.0983	0.224	0.236	0.266	0.212	0.420	0.114	0.195	0.132	0.675	0.534
DE [%R.O.]	0.660	0.320	0.336	0.591	0.294	0.170	0.780	0.633	0.527	0.871	0.447	0.177
RE [%R.O.]	0.358	0.589	1.23	1.10	3.08	4.48	3.04	0.952	4.41	2.04	2.02	2.54
HE [%R.O.]	0.634	0.859	1.69	0.876	1.43	0.639	0.860	0.726	2.04	1.39	1.49	0.517

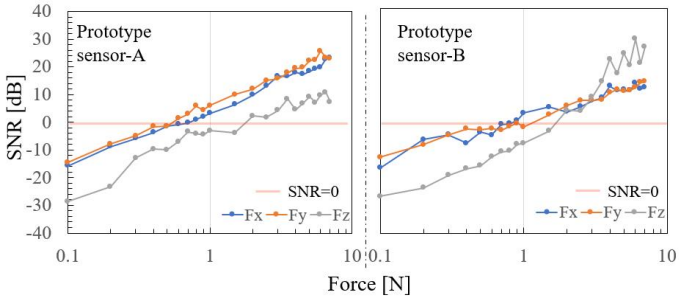

Fig. 14. S/N ratio of prototype sensor-A and B

IV. CONCLUSIONS

Although the potential demand for force sensors is high in both robotics and automation, their usage is still limited to a only few fields owing to their high price. The high price of sensors is mainly owing to the complexity of their manufacturing process. Therefore, a very simple flexure element with holes through the side of a cuboid is proposed to reduce the manufacturing cost of force sensors, and its performance was evaluated. To ensure the safety of the sensor, the influence of the size of the flexure element and load on the maximum von Mises stress was investigated and an approximate equation was obtained. Moreover, the method of attaching a strain gauge to the flexure element to increase the sensitivity of the sensor is described. Consequently, the NE and DE were 0.442 %R.O. and 0.660 %R.O. at maximum, respectively, which is equivalent to those of commercial force sensors. Moreover, based on a comparison of the S/N ratio, the X,Y-axes and Z-axis resolutions were 0.800, 0.600, and 2.00 N, respectively. The difference in the resolutions in the X,Y-axes and Z-axis was solved by adjusting the size of the width and length, and its validity was demonstrated by practically manufacturing another prototype sensor. As a result, the proposed method could be used to develop a force sensor with the same level of performance, while making the cutting process easier compared to conventional methods. This research is expected to lead to lower cost force sensors in the future. While a simple structure offers several advantages, the limited number of design parameters restricts the geometry to meet the required specifications. For instance, this limitation arises when determining the height-to-width ratio of the sensor to achieve isotropic sensitivity.

REFERENCES

[1] S. Chen, Z. Wang, A. Chakraborty, M. Klecka, G. Saunders and J. Wen, "Robotic Deep Rolling With Iterative Learning Motion and Force Control," *IEEE Robot. Automat. Lett.*, vol. 5, no. 4, pp. 5581–5589, Oct. 2020.

[2] Y. Nogi, S. Sakaino and T. Tsuji, "Force Control of Grinding Process Based on Frequency Analysis," *IEEE Robot. Automat. Lett.*, vol. 7, no. 2, pp. 3250–3256, Apr. 2022.

[3] J. Moura, W. Mccoll, G. Taykaldiranian, T. Tomiyama and M. S. Erden, "Automation of Train Cab Front Cleaning With a Robot Manipulator," *IEEE Robot. Automat. Lett.*, vol. 3, no. 4, pp. 3058–3065, Oct. 2018.

[4] S. Weng, Z. Xia, H. Deng, Y. Gan and J. Xiong, "Design of an overload protection device for six-axis force/torque sensors," in *Proc. 2016 IEEE Int. Conf. on Real-time Comput. Robot.*, pp. 239–242, 2016.

[5] L. Fu, A. Song and D. Chen, "A Polyetheretherketone Six-Axis Force/Torque Sensor," *IEEE Access*, vol. 7, pp. 105391–105401, 2019.

[6] J. Yao, L. Zu, H. Ruan, D. Cai, Y. Xu and Y. Zhao, "A heavy load miniature six-component force sening mechanism with hybrid branches," *Measurement*,vol. 157, pp. 107623, 2020.

[7] D. H. Lee, U. Kim, H. Jung and H. R. Choi, "A Capacitive-Type Novel Six-Axis Force/Torque Sensor for Robotic Applications," *IEEE Sensors J.*, vol. 16, no. 8, pp. 2290–2299, Apr. 2016.

[8] S. Somlor, A. Schmitz, H. Jinsun, T. P. Tomo and S. Sugano, "Development of a capacitive-type 6-axis force/torque sensor," in *Proc. 2017 IEEE SENSORS*, pp. 1–3, 2017.

[9] M. Pu, Q. Liang, Q. Luo, J. Zhang, R. Zhao, Z. Ai and F. Su, "Design and optimization of a novel capacitive six-axis force/torque sensor based on sensitivity isotropy," *Measurement*, vol. 203, pp. 111868, 2022.

[10] M. Y. Cao, S. Laws and F. R. y Baena, "Six-Axis Force/Torque Sensors for Robotics Applications: A Review," *IEEE Sensors J.*, vol. 21, no. 24, pp. 27238–27251, Dec. 2021.

[11] J. O. Templeman, B. B. Sheil and T. Sun, "Multi-axis force sensors: A state-of-the-art review," *Sens. Actuators A, Phys.*, vol. 304, pp. 111772, Apr. 2020.

[12] R. Tamura, T. Horikoshi, S. Sakaino and T. Tsuji, "High Dynamic Range 6-Axis Force Sensor Employing a Semiconductor-Metallic Foil Strain Gauge Combination," *IEEE Robot. Automat. Lett.*, vol. 6, no. 4, pp. 6243–6249, Oct. 2021.

[13] M. K. Kang, S. Lee and J. H. Kim, "Shape optimization of a mechanically decoupled six-axis force/torque sensor," *Sens. Actuators A, Phys.*, vol. 209, pp. 41–51, 2014.

[14] J. Yao, H. Zhang, J. Zhu, Y. Xu and Y. Zhao, "Isotropy analysis of redundant parallel six-axis force sensor," *Mech. Mach. Theory*, vol. 91, pp. 135–150, 2015.

[15] Z. Wang, Z. Li, J. He, J. Yao and Y. Zhao, "Optimal design and experiment research of a fully pre-stressed six-axis force/torque sensor," *Measurement*, vol. 46, no. 6, pp. 2013–2021, 2013.

[16] J. H. Kim, D. I. Kang, H. H. Shin and Y. K. Park, "Design and analysis of a column type multi-component force/moment sensor," *Measurement*, vol. 33, no. 3, pp. 213-219, 2003.

[17] I. Payo, J. M. Adánez, D. R. Rosa, R. Fernandez and A. S. Vázquez, "Six-Axis Column-Type Force and Moment Sensor for Robotic Applications," *IEEE Sensors J.*, vol. 18, no. 17, pp. 6996-7004, Sept. 2018.

[18] R. P. Ubeda, S. C. G. Rubert, R. Z. Stanisic and Á. P. Ivars, "Design and Manufacturing of an Ultra-Low-Cost Custom Torque Sensor for Robotics," *Sensors* vol. 18, no. 6 pp. 1786, 2018.

[19] J Yao, H. Zhang, X. Xiang, H. Bai and Y. Zhao, "A 3-D printed redundant six-component force sensor with eight parallel limbs," *Sens. Actuators A, Phys.*, vol. 247 pp. 90–97, 2016.

[20] F. Arai, Y. Murozaki, S. Sakuma, "Improvement of the Measurement Range and Temperature Characteristics of a Load Sensor Using a Quartz Crystal Resonator with All Crystal Layer Components," *Sensors* vol. 17, pp. 1067, 2017.